ELSEVIER

Journal of Applied Geophysics 32 (1994) 347–355

APPLIED GEOPHYSICS

Ray tomography: errors and error functions

J.C. Santamarina, A.C. Reed

Department of Civil Engineering, University of Waterloo, Waterloo, Ont. N2L-3G1, Canada

Received 13 July 1993; accepted 14 July 1994

Abstract

Tomography is the inversion of boundary projections to reconstruct the internal characteristics of the medium between the source and detector boreholes. Tomography is used to image the structure of geological formations and localized inhomogenieties. This imaging technique may be applied to either seismic or electromagnetic data, typically recorded as transmission measurements between two or more boreholes. Algebraic algorithms are error-driven solutions where the goal is to minimize the error between measured and predicted projections. The purpose of this study is to assess the effect of the ray propagation model, the measurement errors, and the error functions on the resolving ability of algebraic algorithms. The problem under consideration is the identification of a two-dimensional circular anomaly surveyed using crosshole measurements. The results show that: (1) convergence to the position of the circular anomaly in depth between vertical boreholes is significantly better than for convergence in the horizontal direction; (2) error surfaces may not be convex, even in the absence of measurement and model errors; (3) the distribution of information content significantly affects the convexity of averaging error functions; (4) measurement noise and model inaccuracy manifest in increased residuals and in reduced convergence gradients near optimum convergence; (5) the maximum ray error function increases convergence gradients compared with the average error function, and is unaffected by the distribution of information content; however, it has higher probability of local minima. Therefore, inversions based on the minimization of the maximum ray error may be advantageous in crosshole tomography but it requires smooth projections. These results are applicable to both electromagnetic and seismic data for wavelengths significantly smaller than the size of anomalies.

1. Introduction

Inversion problems are frequently encountered in engineering and science. Fidelity and quality of inversions are conditioned by the nature of the phenomenon, the quality and extent of available data, the adequacy of the model selected to represent the intervening phenomenon, and the inversion procedure. Accumulated evidence in the literature shows that poor data or a poor inversion model will blur images, add non-existent features, and increase the probability of non-uniqueness.

Wave-based seismic geotomography was proposed in the 1970s to determine the characteristics of geological materials by inverting boundary measurements (e.g. Bois et al., 1972; Ivansson, 1986). The most significant data restrictions in geotomography include limited angular coverage, mixed presence of underdetermined and overdetermined regions, noise in the data, coupled effects of attenuation on traveltime data, inadequate source characterization, and the effects of improper coupling of the transducer to the medium, among others.

Wave-propagation models used in geotomography include straight ray, curved ray, and wave equation modeling. Ray models are applicable when the wavelength is significantly less than the size of the anomaly. If velocity variations throughout the medium are small (less than 20–30%) straight rays may be assumed, otherwise significant ray bending takes place and the inversion problem involves sequential backprojection

SSDI 0926-9851(94)00043-3

and ray-tracing cycles to obtain the solution (Bois et al., 1971; Lytle and Dines, 1980; Gustavsson et al., 1986; Ivansson 1986). Assumptions related to the homogeneity and isotropy of the background medium (which hosts the anomaly) are also included under these model restrictions. On the other hand, when the wavelength λ approaches the size of the anomalies, diffraction takes place and full-wave solutions are preferred (Devaney, 1982; Kak and Slaney, 1988). Williamson (1991) and Williamson and Worthington (1993) showed that ray tomography is applicable when the scale length of the anomaly is at least the radius of the first Fresnel zone. That is, if the average ray length is n wavelengths, the size of the inclusion must be at least $\xi \cdot \lambda \cdot (n)^{0.5}$, where ξ is between 0.5 and 1.

Iterative geotomographic algorithms operate on a discrete medium, where the region to be inverted is divided into pixels and the goal of inversion is to determine the attenuation or slowness at each pixel. If the number of pixels exceeds the number of independent measurements, the problem is underdetermined and the solution is not unique. The restriction of norm minimization may be imposed to solve the problem. Alternatively, the medium could be defined in parametric form, greatly reducing the number of unknowns; this type of "simplified medium" assumption is often a recourse in geophysical exploration. For example, in the case of a circular inclusion within an isotropic homogeneous medium, there are only five unknowns: the velocity of the host background V_{back}, and the inclusion coordinate location X_{inc} and Y_{inc}, size R_{inc}, and velocity V_{inc}. Inversion would seek to identify the combination of these five parameters that minimizes the error between the results of the forward model and the measured boundary data. This method does not benefit from the error-redistribution approach used in algebraic algorithms.

Whether the problem is posed in discrete or parametric form, iterative algorithms are error driven, a factor which affects their resolving ability (Menke, 1989). Menke (1984) studied the resolvability of the position of an inclusion anomaly between two lines of sources and receivers. He found that horizontal resolution was somewhat poorer than the vertical resolution, but that this could be improved by increasing either the density or the angular coverage of sources and receivers. Menke (1984) assumed ray beams of finite width to take into account limited ray bending and the measurement of properties along a finite ray tube.

The purpose of our study was to determine the resolvability of background and anomaly characteristics, the effects of data restrictions, the consequences of the assumed wave propagation model, and the performance of different error functions. The study was restricted to crosshole data and ray models of propagation.

2. Methodology

The case under consideration involved a 2-D circular inclusion centered in a square image region. Tomographic crosshole data were obtained by ensonifying the medium from discrete source positions on one side of the square image zone and measuring projections by means of receivers at discrete positions on the opposite side. The medium was defined in parametric form, $[V_{back}, R_{inc}, X_{inc}, Y_{inc}, V_{inc}]$. The parametric study consisted of determining the global error between measured traveltimes and those traveltimes estimated by forward modeling. Three ray models and three error functions were used.

2.1. Experimental data

Data were obtained in the laboratory using sound waves in air. A 0.23 m radius balloon filled with helium was placed at the center of a 1.5m × 1.5m frame, and crosshole traveltime data were obtained for 16 sources mounted on one side of the frame, and 16 microphones mounted on the opposite side and connected to a multichannel digital storage oscilloscope (Fig. 1). A total of 256 traveltimes were measured. The characteristic wavelength in the background medium was 0.08 m. While the velocity of sound in helium is significantly higher than in air ($v_{He} = 1039$ m/s; $v_{air} = 343$ m/s), first arrivals through the balloon have very low amplitude. Measured traveltimes yielded an actual inclusion velocity, V_{inc}, of approximately 410 m/s.

2.2. Ray models

Three ray models were used. The first was the straight ray model. The second model was a second-order Fourier approximation to the ray equation,

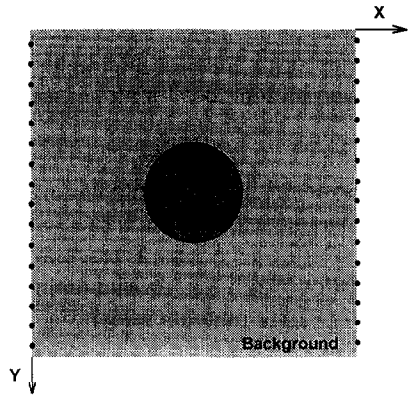

Fig. 1. Circular inclusion in homogeneous background–crosshole tomographic data. Five model parameters [X_{inc}, Y_{inc}, R_{inc}, V_{inc}, V_{back}]. Source signal wavelength: 0.08 m.

whereby a half-sine wave was added to the straight ray. The amplitude of the sine arc was varied until the traveltime was minimized; amplitude is the only parameter optimized in this model. The third ray model represented each ray as a jointed sequence of 16 segments. For a given ray, the initial location of nodes between segments was along the straight line between the source and the receiver. Then, nodes were recursively displaced normal to the straight ray until the traveltime was minimized (Santamarina and Cesare, 1994). For all three models, traveltimes were computed as:

$$t_i = \sum_k \frac{\Delta L_k}{v_k} \tag{1}$$

where t_i is the traveltime i between a given source and receiver, ΔL_k is the length of the ray segment k, and v_k is the velocity along the segment. Straight rays are fastest to compute and easiest to implement in inversion programs as they do not require retracing, i.e. the matrix of travel lengths is computed only once. On the other hand, segmented rays have a large number of degrees of freedom, resulting in computer intensive optimization; yet this model computes the shortest traveltimes.

2.3. Error functions

Three error functions were used to evaluate the global error between measured traveltimes and traveltimes computed for each set of parameters. These error functions are based on the L_1, L_2 and L_∞ norms. L_1 and L_2 norms were divided by the total number of rays n to express the "average residual error per ray" and to facilitate comparison:

$$\text{Average absolute error } E_{abs} = \frac{\sum_i |e_i|}{n} \tag{2}$$

$$\text{Average squared error } E_{sqr} = \sqrt{\frac{\sum_i e_i^2}{n}} \tag{3}$$

$$\text{Maximum ray error } E_{max} = \max |e_i| \tag{4}$$

where e_i is the error for ray i, $e_i = [t_i^* - t_i]$; t_i^* is the predicted traveltime, and t_i is the measured traveltime.

The average squared error E_{sqr} presumes that the data follow Gaussian statistics, and places more emphasis on large magnitude errors than on the absolute error function E_{abs}. The maximum error function selects the single largest error. Standard ART and SIRT algorithms attempt to minimize E_{sqr}. Regardless of the selected error function, the partial derivative of the error function with respect to a parameter, e.g. R_{inc}, gives the component of the gradient that drives the convergence of the solution to the correct value of that parameter.

3. Analysis and results

The invertibility of model parameters [V_{back}, R_{inc}, X_{inc}, Y_{inc}, V_{inc}] depends on the sensitivity of the selected error function to each parameter. Errors between measured and predicted traveltimes are minimized when the model parameters are at or near their true values, i.e. global minimum of the error surface. However, there are differences in evaluation of error functions and rates of parameter convergence, which are dependent on information density, ray model error, and measurement errors. These effects were evaluated using the following procedure: (1) one of the model parameters was varied [V_{back}, R_{inc}, X_{inc}, Y_{inc}, or V_{inc}]; (2) traveltimes were computed for all rays with the selected ray model; (3) the chosen error function was evaluated with respect to the measured traveltimes (Eqs. 2, 3 or 4).

3.1. Error functions

The sensitivity of different error functions to variations in the five parameters was studied with traveltimes obtained from the multi-segment ray model. Results are summarized in Fig. 2. The ray nodes most often do not fall on the boundary between the anomaly and the background medium. This manifests as noise in the error–parameter curves, particularly with geometric parameters X_{inc}, Y_{inc} and R_{inc}. While average error functions reduce these and other effects such as data errors, the maximum error function highlights these effects and may even present local minima (see variation for X_{inc} in Fig. 2).

Error surfaces show different gradients. The maximum ray error function presents the highest gradient for all five parameters, with lower gradients in the average squared error function. Average error functions result in shallow transitions around optimum while the maximum ray error function remains acute (see vari-

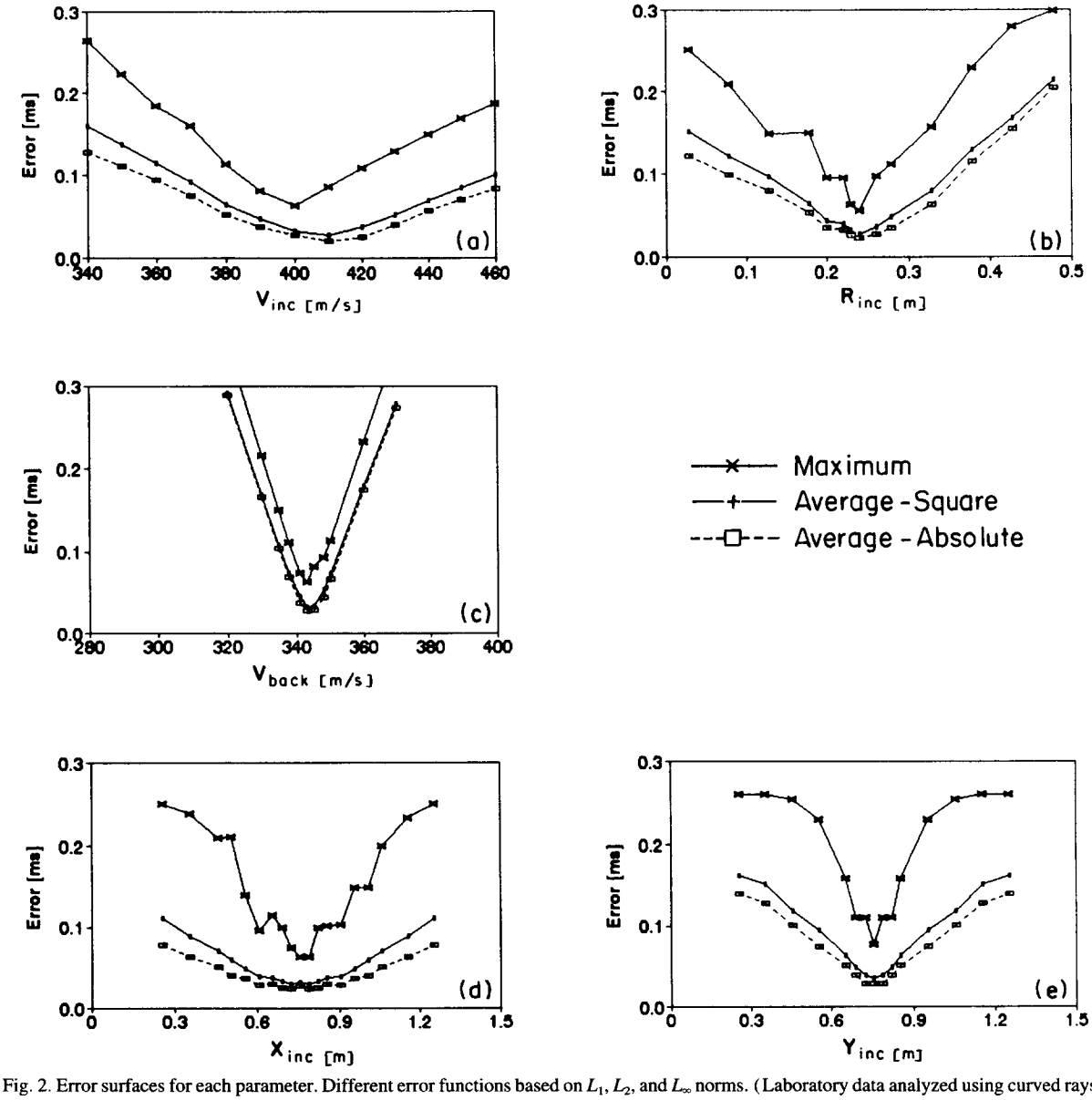

Fig. 2. Error surfaces for each parameter. Different error functions based on L_1, L_2, and L_∞ norms. (Laboratory data analyzed using curved rays).

ation for Y_{inc} in Fig. 2). In summary, error averaging functions appear to be less efficient yet more reliable in guiding the convergence than the maximum function.

3.2. Parameter convergence

Convergence curves are dissimilar for the different parameters, depending upon dimensionless ratios that involve the size and velocity of the inclusion, the separation between boreholes, and the host background velocity. While a comparison at a dimensionless level is more general, the analysis loses clarity and, therefore, comparisons are restricted to dimensionally similar parameters.

The error surfaces for the velocity and size of the inclusion, V_{inc} and R_{inc}, are not symmetrical (Fig. 2a,b): small size or low-velocity contrast imply decreased relative importance of the inclusion with respect to the background. Additionally, in weakly heterogeneous media with only a few small anomalies such as the case under study, the velocity of the background affects all rays, for the majority of their travel distances. Hence, convergence of the background velocity is very steep as shown in Fig. 2c.

Convergence of the vertical position of the inclusion Y_{inc}, in depth between to the instrumented boreholes is significantly better than for the horizontal position X_{inc} (Fig. 2d,e). The incorrect location of the anomaly in the horizontal direction affects mostly the same group of rays which traverse the inclusion in the correct location. Furthermore, the affected rays are deflected by a small range of angles, with limited effect on traveltimes. In contrast, the incorrect Y-location affects a significant number of rays: originally untouched rays may become touched by the inclusion, and those that traverse the inclusion in the correct location may not do so for the new assumed position. As a result, the total residual error increases sharply.

An important consequence of the convergence interpretations stated above is that if the anomaly is assumed to be absent from the region traversed by any ray, the error analysis may lead to a lower total residual error than in the case of a misplaced anomaly. Hence, only rays that traverse the inclusion in its correct position are affected by its absence. Therefore, error averaging functions are not convex, even in the absence of measurement and model errors.

If error maxima fall outside of the region under study defined by the square tomographic image plane, convergence is not affected. However, if error maxima occur inside this region, algorithms may converge to local minima, thus rendering inadequate tomographic images. Geometry is a governing parameter: the larger the relative size of the inclusion, the further away the error maxima boundary is from the correct location of the inclusion. In addition, the coupling between the distribution of information content and the type of error function also affects the convexity of the error surface, as shown next.

3.3. Information density

There are different measures of the information content at a given pixel, such as the number of rays that touch the pixel, the total length of rays across the pixel, and the maximum angle between any two rays across the pixel. The distribution of information content by any of these measures is quite uneven when only crosshole data are available, as shown in Fig. 3. In particular, it can be seen that the information density is very low near the non-instrumented boundaries.

Error averaging functions reflect not only the magnitude of errors for single measurements, but also the number of rays in error. Therefore, as the assumed location of the inclusion approaches the boundaries where the number of rays decreases, the magnitude of the average error functions also decreases. On the other hand, the maximum error function reflects the value of the worst traveltime error, regardless of the number of rays in error. Thus, the maximum ray error function is expected to be more stable with respect to information content.

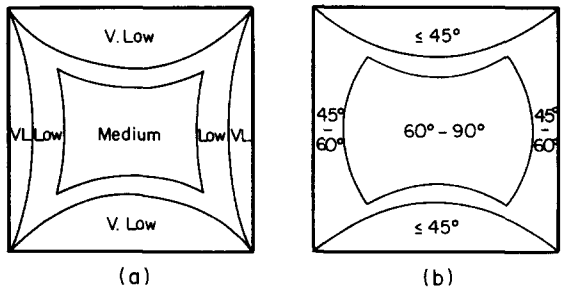

Fig. 3. Distribution of information content within the unknown space for the crosshole configuration. (a) Total travel length per pixel. (b) Maximum angularity of any two rays traversing the pixel.

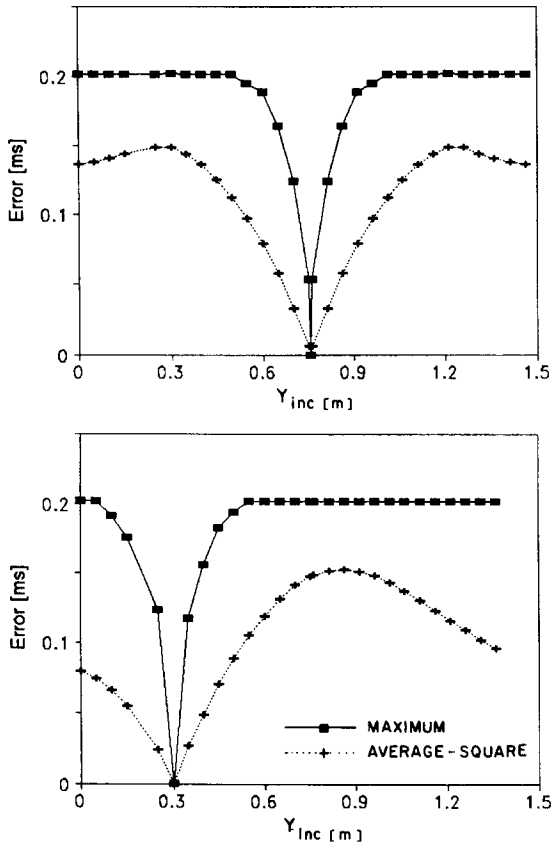

Fig. 4. Effect of information content on error surfaces. Inclusion at two locations: $Y_{inc} = 0.3$ m and $Y_{inc} = 0.75$ m. Averaging error functions reflect distribution of information. (Simulated data analyzed using curved rays).

The combined effect of information content and error function was studied only in reference to the vertical location of the inclusion, Y_{inc}. Two different "known" vertical positions of the anomaly were assumed: $Y_{inc} = 0.3$ m and the standard value used previously, $Y_{inc} = 0.75$ m. Computed traveltimes for all other inclusion locations are compared to the traveltimes of these two locations. The resulting average-square and maximum error functions are plotted in Fig. 4. As shown, the low information density at the top and bottom boundaries produce error maxima within the region of interest when the average error function is used. On the other hand, the maximum ray error function remains constant away from optimum. Local maxima may significantly mislead error driven algorithms searching for off-center anomalies; indeed, there is a high probability that the algorithm will place the anomaly on the opposite side.

Note that for the given model parameters used in this simulation, no significant differences between the convergence gradients near optimum are observed between the two anomaly positions. The error functions are zero at optimum convergence in each case because the computed traveltimes for the misplaced anomaly are compared with respect to the computed traveltimes for the assumed correct location (i.e. no model or measurement error involved).

3.4. Model error

The three ray models (straight ray, sine arc, and multi-segment) were used to study the effect of model error on convergence. The average squared error function and the laboratory data are used in the comparison. Results are shown in Fig. 5. In general, the smaller minimum error indicates that the model more closely approximates the true ray propagation, whereas steeper error gradients between the ray models for the same parameter indicate that the particular model shows greater sensitivity to the parameter.

General trends are similar for all models. It was expected that the multi-segment model would present not only lower minima, but also steeper gradients. While this was observed, the actual differences are relatively small. The sine arc and the multi-segment ray models correspond closely to each other; such an agreement is not expected in asymmetrical problems or in the case of multiple anomalies. The straight ray model leads to the highest minima and slightly lower error gradients since it does not optimize the ray paths as the other two models do.

The greatest inversion discrepancy is for the inclusion size, i.e. the value of R_{inc} corresponding to the lowest point on the error surfaces. In this case, the straight ray model predicts a significantly larger inclusion than the true value, whereas the inclusion size is accurately predicted by the two curved ray models: $R_{inc} = 0.28$ m instead of 0.23 m. This is in agreement with prior observations that showed that straight ray tomography enlarges high-velocity anomalies (Potts and Santamarina, 1993)

3.5. Measurement error

Results presented in Figs. 2 and 5 were obtained by comparing predicted traveltimes with measured trav-

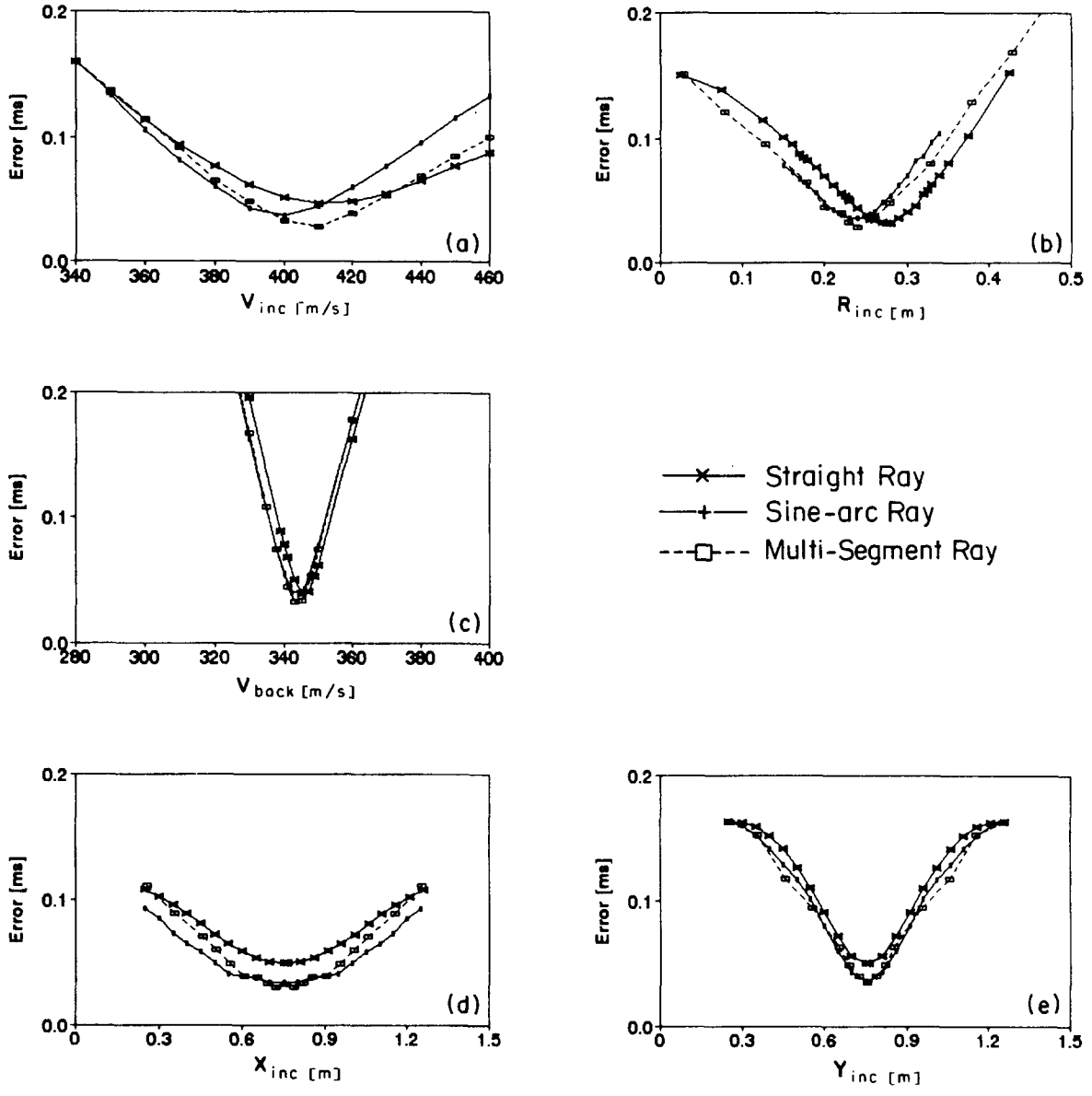

Fig. 5. Model error in forward model: effect on error surfaces. Note that straight rays overestimate size of high-velocity anomalies. (Laboratory data analyzed using curved rays).

eltimes. Real data include measurement errors which result from uncertainty in the location of sources and receivers, source signal triggering jitter, inadequate coupling, and the inherent effect of attenuation in the determination of first arrivals, among others.

The disparity between measured and predicted traveltimes involves both measurement errors and model errors. Thus, in order to study the effect of measurement errors alone, measured traveltimes for the centered inclusion were simulated with the curved-ray model. Traveltimes for off-center positions were computed with the same model, and noise was added. That is:

$$t_i^{\text{error}} = [1 + rnd(\epsilon^-, \epsilon^+)] \cdot t_i \quad (5)$$

Finally, the average square error was computed. Results for the effect of measurement error on the resolvability of Y_{inc} are shown in Fig. 6 for three levels of noise ϵ: 0, 2, and 5%. A conclusion from these results

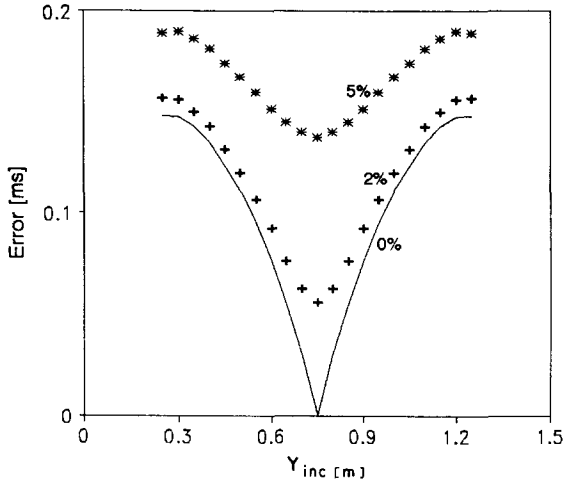

Fig. 6. Error surface for *Y*-location of inclusion as a function of measurement noise. (Simulated data analyzed using curved rays).

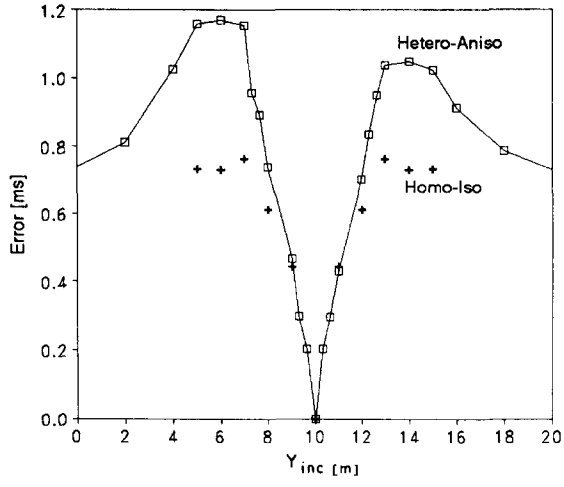

Fig. 7. Error surface for *Y*-location of inclusion in homogeneous–isotropic (*Homo-Iso*) and in vertically heterogeneous–anisotropic (*Hetero-Aniso*) background. (Simulated data analyzed using curved rays).

is that measurement errors raise the error surface, reduce convergence gradients, and reduce the curvature around optimum, thus diminishing the ability to resolve the anomaly.

3.6. *Heterogeneous–anisotropic background*

The impact of changing the homogeneous isotropic background medium to a vertically heterogeneous anisotropic medium on the resolvability of the vertical location of an inclusion was investigated. This is a more relevant background in particulate materials such as soils. A 2 m diameter inclusion was moved vertically along the central axis of a 10 m wide by 20 m simulated deep soil formation. In the first case, the medium is vertically heterogeneous and anisotropic, having the following seismic velocity field:

$$V_v(z) = a + \beta \cdot z^x = 150 + 150 \cdot z^{0.2}$$

$$V_h(z) = \delta \cdot V_v = 0.8 \cdot V_v(z) \qquad (6)$$

where z is in m and the horizontal and vertical velocities are in m/s. For comparison, the medium in the second case is isotropic and homogeneous, with velocity equal to the average velocity at depth of 10 m in the previous case, $V_{back} = 388$ m/s. Simulated traveltimes were computed with the multi-segment algorithm, which is designed to find optimal ray paths in vertically heterogeneous, anisotropic media (Santamarina and Cesare, 1994). Results computed with the average square error function are presented in Fig. 7. In the case of the vertically heterogeneous anisotropic background, the error at shallower depth is greater than the error at greater depth because the larger velocity contrast between the inclusion and the background at shallower depth. The flattening and decrease of the curve at the extremes reflects that the inclusion is entering regions of low information content and should lead to error values equal to that of the absent inclusion case. The comparison with the homogeneous isotropic material shows virtually no difference around optimum. Away from optimum, convergence gradients in the homogeneous–isotropic case are lower since the velocity contrast between the medium and the anomaly remain constant.

The background medium described by Eq. 6 is a four-parameter medium $[\alpha,\beta,\chi,\delta]$ rather than the one-parameter homogeneous isotropic medium previously discussed. In this case, the error surfaces for the four parameters will require more study to evaluate the convergence of inversion algorithms. The study conducted by Santamarina and Cesare (1994) showed that it is not possible to separate the contribution of anisotropy δ from vertical heterogeneity $[\alpha,\beta,\chi]$, at least for the range of parameters frequently encountered in particulate media.

4. Conclusions

Results from this study are valid for the inversion of transmission traveltime measurements, conducted

using either seismic or electromagnetic waves, when wavelengths are significantly smaller than the size of anomalies. The main conclusions are:

The iterative solution of inversion problems is error driven. Therefore, the error surface determines convergence and resolving ability of the algorithm.

Convergence to the depth position of the inclusion anomaly between the instrumented boreholes is significantly better than for the position in the lateral direction between the instrumented boreholes. The convergence of background velocity is very steep.

Error surfaces may not be convex functions of the parameters of the medium even in the absence of measurement and model errors. Geometric characteristics, the distribution of information content, and the type of error function determine the convexity of the error surface.

Error averaging functions reduce the effects of measurement noise and the consequent possibility of local minima. The maximum ray error function increases the curvature at the minimum, has high convergence gradients, and is unaffected by the distribution of information content.

Measurement noise and model inaccuracy manifest in increased residuals and in reduced convergence gradients near optimum. Resolvability is reduced and the inverted solution may be inadequate.

Anisotropy and vertical heterogeneity in the representative soil background host medium studied seem not to affect, and may even enhance, the error surface for accurately locating the vertical position of anomalies. However, inversion may not distinguish anisotropy from vertical heterogeneity in typical near-surface conditions.

Acknowledgements

This study is part of a research program on wave-material interactions and applications. Support is provided by the Natural Sciences and Engineering Research Council of Canada (NSERC) and industry.

References

Bois, P., La Porte, M., Lavergne, M. and Thomas, G., 1971. Essai de détermination des vitesses sismiques par mesures entre puits. Geophys. Prospect., 19: 42–83.

Bois, P., La Porte, M., Lavergne, M. and Thomas, G., 1972. Well-to-well seismic measurements. Geophysics, 37: 471–480.

Devaney, A.J., 1982. A filtered back propagation algorithm for diffraction tomography. Ultrasonic Imaging, 4: 336–350.

Gustavsson, M., Ivansson, S., Morén, P. and Jörgen, P., 1986. Seismic borehole tomography—Measurement system and field studies. Proc. IEEE, 74: 339–346.

Ivansson, S., 1986. Seismic borehole tomography—Theory and computational methods. Proc. IEEE, 74: 328–338.

Kak, A.C. and Slaney, M., 1988. Principles of Computerized Tomographic Imaging. IEEE Press, New York, NY.

Lytle, R.J. and Dines, K.A., 1980. Iterative ray tracing between boreholes for underground image reconstruction. IEEE Trans. Geosci. Remote Sensing, 18: 234–240.

Menke, W., 1984. The resolving power of cross-borehole tomography. Geophys. Res. Lett., 11: 105–108.

Menke, W., 1989. Geophysical Data Analysis: Discrete Inverse Theory. Academic, Toronto.

Potts, B.D. and Santamarina, J.C., 1993. Geotechnical tomography: The effects of diffraction. ASTM Geotechn. Test. J., 16: 510–517.

Santamarina, J.C. and Cesare, M., 1994. Tomographic Inversion in Vertically Heterogeneous, Anisotropic Media. Dep. Civ. Eng., Univ. Waterloo, Waterloo.

Williamson, P.R., 1991. A guide to the limits of resolution imposed by scattering in ray tomography. Geophysics, 56: 202–207.

Williamson, P.R. and Worthington, M.H., 1993. Resolution limits in ray tomography due to wave behavior: Numerical experiments. Geophysics, 58: 727–735.